Respiratory rhythm modulates membrane potential and spiking of non-olfactory neurons

Maxime Juventin, Mickael Zbili, Nicolas Fourcaud-Trocmé, Samuel Garcia, Nathalie Buonviso, Corine Amat

RESEARCH ARTICLE

RUNNING HEAD: Respiratory modulation in the brain: deep in the cells

ARTICLE TITLE: Respiratory rhythm modulates membrane potential and spiking of non-olfactory neurons

AUTHORS: Maxime Juventin[1], Mickael Zbili[1, 2], Nicolas Fourcaud-Trocmé[1], Samuel Garcia[1], Nathalie Buonviso[1] and Corine Amat[1]

AFFILIATION:

[1] Université Claude Bernard Lyon 1, CNRS, INSERM, Centre de Recherche en Neurosciences de Lyon CRNL U1028 UMR5292, F-69500, Bron, France

[2] Université Clermont Auvergne, CHU Clermont-Ferrand, INSERM, Neuro-Dol, F-63100, Clermont-Ferrand, France

CORRESPONDING AUTHOR: Corine Amat: corine.amat@univ-lyon1.fr

UCBL, CNRS, INSERM, CRNL U1028 UMR5292
Centre Hospitalier Le Vinatier - Bâtiment 462 - Neurocampus Michel Jouvet
95 boulevard Pinel
69675 Bron Cedex
France

26

ABSTRACT

In recent years, several studies have shown a respiratory drive of the local field potential (LFP) in numerous brain areas so that the respiratory rhythm could be considered as a master clock promoting communication between distant brain locations. However, outside of the olfactory system it remains unknown whether the respiratory rhythm could shape membrane potential (MP) oscillations. To fill this gap, we co-recorded MP and LFP activities in different non-olfactory brain areas: medial prefrontal cortex (mPFC), primary somatosensory cortex (S1), primary visual cortex (V1), and hippocampus (HPC), in urethane-anesthetized rats. Using respiratory cycle-by-cycle analysis, we observed that respiration could modulate both MP and spiking discharges in all recorded areas during episodes that we called Respiration-Related oscillations (RRo). Further quantifications revealed that RRo episodes were transient in most neurons (5 consecutive respiratory cycles in average). RRo development in MP was largely correlated with the presence of respiratory modulation in the LFP. By showing that the respiratory rhythm influenced brain activities deep to the MP of non-olfactory neurons, our data support the idea that respiratory rhythm could mediate long-range communication between brain areas.

NEW & NOTWORTHY

In this study, we evidenced strong respiratory driven oscillations of neuronal membrane potential and spiking discharge in various non-olfactory areas of the mammal brain. These oscillations were found in medial prefrontal cortex, primary somatosensory cortex, primary visual cortex and hippocampus. These findings support the idea that respiratory rhythm could be used as a common clock to set the dynamics of large-scale neuronal networks on a same slow rhythm.

KEY WORDS: freely breathing anesthetized rat, intracellular activities, local field potential, membrane potential, respiration-related oscillations.

INTRODUCTION

In recent years, a resurgence of publications has proposed respiration as a master clock for brain rhythms, following many observations that reported the breathing rhythm as being able to modulate complex behaviors or cognitive process (1–4). The exploratory behavior of rodents, consisting in rhythmical sampling of the environment, is a perfect example since the onset of each respiratory cycle initiates a "snapshot" of the orofacial sensory environment, comprising sniffing, whisking and head movements (5–7). Similarly, licking synchronizes with breathing (8, 9). In humans, respiration modulates memory consolidation (10), associative learning (11), cognitive performances (12–14), sensory perception (15, 16), and motor behaviors (17, 18). Respiratory phase influences the initiation of a voluntary action (19) or a cognitive task and its performance (13). All these data therefore suggest that the brain could have at least one processing mode depending on the respiratory phase.

Parallel to this literature on the effects of breathing on behavior has appeared an equally important literature on a respiratory drive of brain activity, both in human and rodent. In humans, intracerebral EEG-breathing coherence has been observed particularly in the hippocampus, amygdala, insula and the parietal lobe (14, 20) and the inhalation phase is correlated with an increase in the power of delta oscillations (14). In rodents, a respiration-locked local field potential (LFP) oscillation has been described in the hippocampus (21), the somatosensory cortex (22), the prefrontal cortex (23, 24), neocortical regions as posterior as visual cortex and even subcortical areas (25, 26). Breathing also modulates other rhythms in several brain regions. In the hippocampus, the timing of hippocampal sharp-waves and ripples is respiration-coupled (27, 28). In the somatosensory cortex, delta oscillations are respiration-locked whereas gamma power is respiration-modulated (22). In the prefrontal cortex, fast gamma LFP oscillations (29) and unitary activities (23) are phase-coupled with respiration.

This respiratory drive, described in such a large cerebral network, is at the moment assumed to arise via the activation of the olfactory bulb (OB) *via* mechanical stimulation of olfactory receptor cells by nasal respiratory airflow (30). Indeed, respiration-brain activity coupling dissipates in human when subjects breathe through the mouth (14) or in rodents when OB is silenced (21, 22, 28, 31). This respiration-related activity was first found in the OB where it has been largely described (For review, see (1)): respiration modulates both LFP and individual cells activities, including spiking discharge and membrane potential dynamics. In LFP signal, fast rhythms occurrence is shaped by the slow respiration-related oscillation (RRo), beta and gamma waves alternating on expiratory and inspiratory phases, respectively (33, 34). Mitral/tufted cells spiking discharge is strongly patterned by respiratory rhythm both in anesthetized (34–37) and awake rodent (38, 39). Importantly, even the membrane potential of mitral/tufted cells is influenced by respiration (35, 40, 41). Particularly, RRo of membrane potential constrain fast oscillations to occur concomitantly with LFP signal, hence favoring interaction between fast LFP and spiking (41). We and others have demonstrated that most of OB respiratory modulation is related to the amplitude of the inspiratory airflow (36, 42–44). Respiratory influence is also present, to a lesser extent, in the olfactory cortex both at the LFP and cellular levels (Piriform cortex: (1–4); Olfactory tubercle: (49)). Directly in contact with nasal respiratory airflows, the olfactory system is thus strongly impacted by respiration dynamics.

Oppositely, while LFP activity in non-olfactory regions has been described as respiration-modulated, very little is known about respiratory modulation of individual cell activities. Only a few reports described spiking discharge (extracellularly recorded) modulated by respiration (23, 24). Only one article reported intracellular recordings in parietal cortex (50). The authors showed membrane potential oscillations that were coherent with respiration in 6 out of 29 parietal neurons, no further studies were done. Here we asked to what extent respiratory

modulation could shape cellular activity, including MP and spiking activity, in non-olfactory areas. To this purpose, we co-recorded membrane potential and LFP activities in widespread brain areas, namely the medial prefrontal cortex (mPFC), the primary somatosensory cortex (S1), primary visual cortex (V1), and hippocampus (HPC), in urethane-anesthetized rats. Using respiratory cycle-by-cycle analysis, we tracked respiratory modulation of cellular activities. We observed that both MP and spiking discharges could be respiration-modulated in all recorded areas, but more transiently than what we previously described in the OB (35). Particularly, respiratory modulation of MP was highly variable both between structures and between cells, very transient for most of cells and largely influenced by LFP state. Finally, moderate hyperpolarization of MP reduced the probability of RRo.

118 MATERIALS AND METHODS

119 Experimental procedures

120 *Animal care*

121 The 25 male Wistar rats (325.2±32.1g, Charles River) used were housed in groups of four in a
122 temperature (22±1 ◦C) and humidity (55±10%) controlled room and exposed to a 12/12 h
123 light/dark cycle (light onset, 6:00 am). Experiments were conducted during the light period
124 (between 9:00 am and 3:00 pm). Food and water were available *ad libitum*. All experiments
125 were carried out in accordance with Directive 2010/63/EU of the European Parliament and of
126 the Council of the European Union regarding the protection of animals used for scientific
127 purposes and in compliance with the ARRIVE guidelines. The experimental protocols were
128 approved by the National Ethics Committee "Animal Experimentation Committee of Univ.
129 Claude Bernard Lyon 1—CEEA-55" (Agreement APAFIS #17088).

130 *Animal preparation*

131 Rats were anesthetized with an intraperitoneal injection of urethane (1.5 g/kg), then, placed in
132 a stereotaxic apparatus. Respiration was recorded with a homemade bidirectional airflow
133 sensor placed at the entrance of the right nostril. Positive and negative flows corresponded
134 respectively to inspirations and expirations. Body temperature was kept at 37 °C using a
135 heating pad (Harvard Apparatus, Holliston, MA USA). A craniotomy of about 3x3 mm was
136 performed above the site of recording: medial prefrontal cortex, primary visual cortex,
137 somatosensory barrel cortex or hippocampus. Dura was removed, and Ringer's lactate
138 solution was regularly applied onto the brain to prevent from drying. At the end of the
139 experiments, rats were euthanized by intracardiac injection of Dolethal©.

140 *In vivo Electrophysiological Recordings*

We made simultaneous intra- and extracellular recordings in freely breathing anesthetized rats. Intracellular recordings (n = 69 cells) were performed in four different areas of the left hemisphere: the medial prefrontal cortex (mPFC, AP: 3.1±0.4 mm, MD: 0.7±0.2 mm), the primary somatosensory cortex (S1, AP: -2.4±0.4 mm, MD: 5.0±0.1 mm), the primary visual cortex (V1, AP: -5.3±0.2 mm, MD: 4.5±0.8 mm) and the hippocampus (HPC, -3.5±0.7 mm, MD: 2.6±0.7 mm). Input resistance of the neurons was 52.7 ± 4.7 MΩ (Supplemental Figure S1). Borosilicate glass capillaries (o.d. = 1.5 mm; i.d. = 0.86 mm, Harvard Apparatus, Holliston, MA, USA) were pulled with a horizontal puller (model P-97, Sutter Instruments, Novato, CA, USA). The micropipettes were filled with a 2 M potassium acetate solution, and their resistances ranged from 50 to 120 MΩ. Microelectrodes were lowered using a piezo manipulator (PM-10, World Precision Instruments, Sarasota, FL, USA). The electrophysiological signal was amplified and low-pass filtered at 10 kHz by an intracellular amplifier (Axoclamp 2B, Axon Instruments, Foster City, CA, USA). Local field potential (LFP) was recorded simultaneously with intracellular signal using silicon probes (Neuronexus Technology, Ann Arbor, MI, USA) placed as close as possible to the glass microelectrode. The signal was amplified, and low-filtered at 5 kHz with a homemade amplifier. Respiration was recorded with an airflow sensor (described in (51)). Positive and negative values corresponded to expiration and inspiration respectively. All signals were then digitalized at 25 kHz (NI USB-6211, National Instruments, Austin, TX, USA) and stored on a computer using Neurolabscope, a homemade software.

Internal polarity state

Internal polarity states were encoded based on the sign (positive or negative) and intensity of direct current (DC) injection, amplitude of MP variation and firing activity. We identified 4 states: strong hyperpolarization (Hyp2), light hyperpolarization (Hyp1), basal level (Base), depolarization (Dep). A given cell was not systematically recorded in each of the 4 states.

Post hoc verification confirmed our classification (Supplemental Figure S2). Whatever the structure, basal level (Base) represented the state where no (N = 42 cells) or a very low stabilizing current (-0.07±0.06 nA, N = 14 cells) was injected. Hyp1 level corresponded to a MP hyperpolarization of around 7 mV relative to the basal level, at which the spike discharge decreased by around 60%. This level was reached with a -0.29±0.04 nA (N = 25 cells) DC injection. Hyp2 level corresponded to a MP hyperpolarization of around 12 mV relative to the basal level, at which the spike discharge decreased by 90% to 100%. This level was reached with a -0.42±0.04 nA (N = 31 cells) DC injection. Dep level corresponded to a MP depolarization of around 7 mV relative to the basal level, at which the spike discharge increased by at least 10%. This level was reached with a 0.19±0.03 nA (N = 21 cells) DC injection. For the cell-by-cell analysis, in order to limit the influence of external factors, we selected pair of recordings close in time. In the mPFC, cells (N = 9 cells) received -0.17±0.02 nA for Hyp1, resulting in a hyperpolarization of 7.6±2.5 mV and a decrease in spike discharge of 74.4±7.5 %. Latency between Base and Hyp1 recordings was 3.2±1 min. In S1, cells (N = 4 cells) received -0.19±0.06 nA for Hyp1 resulting in a hyperpolarization of 8.4±5.2 mV and a decrease spike discharge decrease of 50.0±26.6 %. Latency between Base and Hyp1 recordings was 3.3±1.4 min. In HPC, cells (N = 3 cells) received -0.26±0.05 nA for Hyp1 resulting in a hyperpolarization of 7.6±3.0 mV and a decrease in spike discharge of 50.5±10.0 %. Latency between Base and Hyp1 recordings was 1.3±0.2 min.

Data analysis

All following analyses have been made using homemade Python scripts.

Respiratory signal processing

Respiratory cycles were detected as previously described in (51). Respiration was monitored with an airflow sensor. Positive, respectively negative, values corresponded to expiration,

respectively inspiration. Null values corresponded to transition between inspiration and expiration. Briefly, respiratory signal was low-pass filtered (8Hz) to reduce noise, then zero-crossing points were detected to delineate the start points of inspiration and expiration. Finally, the time of each respiratory cycle was linearly converted to phases ranging from 0 to 1. In summary, all respiratory cycles were detected, inspiration and expiration phases were well determined, and respiratory phases were computed.

Rescaling time basis of signals with respiratory phase

We wanted to track variations in the signals of interest (LFP, MP, AP discharge) in relation to respiratory rhythm. However, respiratory cycles exhibited variability in duration, and the inspiration-expiration ratio in two cycles with similar duration may be different. The respiratory phase is therefore the appropriate time scale for reducing jitter due to respiratory cycle variability. Following (51), we rescaled the signals of interest as a function of the respiratory phase. Briefly, after detecting the respiratory cycles, the signal for each cycle was interpolated into a 2000-points vector. To account for the asymmetry of respiratory cycles, the average inspiration ratio (inspiration duration/cycle duration) was computed for each recording. Cycle by cycle interpolation preserved the ratio, *i.e.,* for a 0.33 ratio, interpolation attributed 33% of the 2000 points to the inspiration period and the remainder to the expiration period. This rescaling allowed the construction of respiration-triggered MP average (Figure 2C bottom) or respiration-triggered AP histogram (Figure 2C top). We made one exception to construct Figure 4B as we wanted to compare the preferred phase of depolarization between cells, so we rescaled all recordings with the same ratio 0.4 in order to align all cell respiratory phases. The average inspiration-expiration ratio of our dataset was 0.41±0.01.

Time dynamics of respiration-related oscillations

In this section, we will describe how we detected **respiration-related oscillations (RRo)** in oscillatory signals (membrane potential and LFP). We proceeded in 5 steps (Figure 1A).

(i) Preprocessing and deformation to respiratory phase. For the membrane potential, preprocessing consisted in removing the APs, in order to focus on membrane potential oscillations. As the duration of APs in our population of neurons was homogeneous (Supplemental Figure S3), we used the same cutting values for all our neurons. To remove APs, single APs were cut from 4 ms before to 5 ms after the peak while bursts (defined by interspike interval < 20ms) were cut from 30 ms before the first AP to 30 ms after the last AP. The cut signal was replaced by a linear interpolation between the two extremities. For the LFP, preprocessing consisted in high-pass filtering (0.1 Hz). Once preprocessed the signal of interest was deformed to respiratory phase (see *Rescaling time basis of signals with respiratory phase).*

(ii) Detection of synchronization with respiration in local windows. As we wanted to track the temporal dynamics of respiration-related oscillations, we scanned the recordings with windows of 4 respiratory cycles, with an overlap of 3 cycles between consecutive windows (Figure 1B.2). For each window, we computed the median signal from the 4 respiratory cycles (example in Figure 1C.2 left, green trace), which represented a proxy for estimating a local oscillation at respiratory frequency. To assess the importance of the respiratory modulation, we measured the amplitude of this median signal (example in Figure 1C.2 left, red bar), which is expected to be high when the oscillations are synchronized with the respiration. To test the significance of such a local respiration-related oscillation, we compared the actual amplitude with amplitudes of 500 surrogates (example in Figure 1C.2 and C.3). We considered the oscillation of the windows to be respiration-related if the actual amplitude was larger than 95th percentile of surrogate amplitudes (example in Figure 1C.3). The construction of the surrogates (see Figure 1C.1) consisted in creating pairs of cycles (cycles 118&119, and

121&120 in our example Figure 1C.1), and then phase-shifting the signal. For one pair, we shifted the first cycle with a random phase (φ_1). The other cycle of the pair was shifted in phase opposition ($\varphi_1+\pi$). We repeated this transformation for the second pair of cycles with another random phase shift (φ_2). This manipulation neutralized the respiratory component of the signal.

(iii) Verification of the similarity between individual cycles and local oscillation. From the windows previously identified as respiration-related (windows 118 to 120 in our example Figure 1B.2), we wanted to identify the cycles that actually contributed to this respiration-related oscillation. To verify that individual cycles within the window were similar to the local waveform, we computed the scalar product of each cycle with the window median signal (example for one cycle in Figure 1D.1). Since we focused on the waveform, not on the amplitude, we z-scored the signals before performing the scalar product. We assessed the significance by comparing the scalar product of actual data with the scalar product from the 500 surrogate window signals (Figure 1D.1 and D.2). We considered the individual cycle significantly similar to the local waveform if the scalar product value was greater than the 95^{th} percentile of surrogated scalar product values (detailed histogram for cycle 118 with window 118 in Figure 1D.2).

(iv) Cycle by cycle encoding. To switch toward a cycle-by-cycle encoding, we wanted to make sure that the individual cycles, constituting the windows previously identified as respiration-related, actually displayed respiration-related oscillations. To do so we scored each cycle as follows. Each time the Vm of a cycle was similar (black rectangle in Figure 1B.3) to the waveform of a respiration-related window (red windows in Figure 1B.2), the score was incremented by one. For example, the cycle 121 (Figure 1B.3) participated in three windows identified as respiration-related (windows 118-120). The cycle 121 was similar to the waveforms of these 3 respiration-related windows and was not tested for the non-

modulated (window 121). The cycle 121 reached the score of 3. Since a cycle can be scanned up to four times (in four consecutive windows), score of a cycle ranged from 0 to 4. We classified cycles in three respiration-related categories as follows: 0 and 1: non-modulated cycles, 2: undetermined, 3 and 4: modulated cycles. In our example (see Figure 1B.4) cycles 120 and 121, with a score of 3, were then considered as RRo.

(v) Curation of isolated events. Finally, we eliminated all single or doublet cycles identified as RRo, and they were reassigned to the undetermined category. Indeed, we considered that respiratory related episodes lasting less than 3 consecutive cycles were not statistically relevant and too much susceptible to false detection.

For each recording, we were then able to compute the probability of RRo (expressed in percent), defined as the ratio between the number of respiratory cycles with respiration-related oscillations and the total number of cycles. This probability was not biased by the recording duration (Supplemental Figure S4A, which varies from cell to cell), the absolute respiratory frequency (Supplemental Figure S4B, proxy for depth of anesthesia), the input resistance of the cells (Supplemental Figure S4C). On the contrary, the RRo probability was correlated with coherence to respiration (Supplemental Figure S4D, $p = 5.6.10^{-16}$).

We performed a last refinement to identify **respiration-modulated cells or LFP:** For further quantification of membrane potential or LFP respiration-related dynamics, we wanted to keep only **cells or LFP** recordings that were significantly synchronized with respiration. If we considered every recording for which RRo were detected as an overall respiration-modulated recording, longer recordings would present greater chance to be defined as “respiration-modulated”. Therefore, to counterbalance this bias, we computed a cell-by-cell threshold on the proportion of required RRo cycles in order to classify the cell or LFP recording as respiration-modulated. To do so, for each recording, we first estimated the respiratory

frequency by taking the peak frequency from the respiration power spectrum. The breathing rhythm being extremely stable during anesthesia, a narrow notch filter (mne.notch filter, 'spectrum_fit' method, notch width = 1 Hz, mne version 0.20.1) applied on the signal of interest (membrane potential or LFP) removed the respiratory component of the signal, while preserving the other oscillations. The signal was then randomized using Fourier phase randomization technique. Spurious respiration-related oscillations were detected with the previously described algorithm. These steps were repeated 200 times. The number of cycles with respiration-related oscillations detected out of the 200 respiration-deprived signals were gathered and, the 95^{th} percentile was computed. This percentile represented our threshold of significance. If the number of cycles with respiration-related oscillation detected on the true signal was above the threshold, we considered the recording as respiration-modulated. As a result, this selection excluded one V1 neuron from our Base polarity population, (indicated with the black cross on cell 3 from V1 in Figure 3A). One cell in HPC was excluded from Hyp1 population. Two cells in HPC were excluded from Hyp2 population.

Respiration-triggered membrane potential

Using the classification method described previously, we could isolate membrane potential cycles related to respiration. These cycles were then stacked, and we computed the median signal. For each respiration-modulated cell, the amplitude of respiration-related oscillations was defined as the maximum/minimum difference of this median signal. To analyze the depolarization preferred phase, we computed the median respiration-triggered signal, then we extracted the mean vector from which we finally measured the angle. For this latter analysis we only used RRo cycles of respiration-modulated cells.

Respiration-triggered spiking pattern

AP times were rescaled to a respiratory cycle phase basis. Therefore, AP were identified by the number of the respiratory cycle they belong to, and their respiratory phase within that cycle. Once respiratory cycles were classified in respiratory-related categories, we could sort AP according to these categories. Then, for each cell and each respiratory-related category we built a respiration-triggered discharge histogram. For each cell, three experts, independently, visually encoded spiking patterns associated to each respiratory-related category. Spiking patterns were classified as: respiration-related, not respiration-related, or undetermined (not enough spikes to conclude). This classification was inspired from (32).

Power spectrum

For the 4 examples in Figure 2, Morlet wavelet time-frequency maps (0.4-6Hz) for respiratory signal and AP-removed membrane potential were computed for whole recordings. We then extracted the 4-second time windows showed in the figure and averaged across time to estimate the power spectrum. Spectra were normalized by their sum to obtain a density.

Extracellular signal (LFP) processing

The LFP signal was 0.1 Hz high pass filtered. Then, similarly to membrane potential oscillations, LFP-respiration relationship was classified cycle by cycle. Using this classification, the relationship to respiratory rhythm was then compared between membrane potential and LFP.

Conditional probabilities

For this analysis, we kept recordings for which both membrane potential and LFP exhibited significant respiration-modulation (as described in *Time dynamics of respiration-related MP oscillations*). In Figure 5D, we examined the conditional probability to observe membrane potential RRo in relation to LFP dynamics. In other words, we split recording according to the

LFP RRo encoding. On the one hand we computed membrane potential RRo probability among cycles with LFP RRo. On the other hand, we again computed the membrane potential RRo probability among cycles during which LFP activity was not related to respiration (other LFP activity). Figure 5E is the complementary view, since we computed the conditional probability to observe LFP RRo according to membrane potential dynamics (RRo versus other activity).

Statistics

Statistics were made with Scipy (version 1.4.1) python package (scipy.stats.wilcoxon, scipy.stats.mannwithneyu, scipy.stats.kruskal). All averages are presented under the format mean ± SEM. Where this is not the case, it is explicitly stated.

346 RESULTS

347 **Evidence of respiratory modulation of cell membrane potential in non-olfactory**
348 **structures**

349 *In vivo* intracellular activities recordings were obtained from 4 non-olfactory structures in 25
350 freely breathing anesthetized rats; all polarity states combined, 34 cells were recorded in
351 medial prefrontal cortex (mPFC, N = 9 rats), 13 cells in somatosensory cortex (S1, N = 4
352 rats), 5 cells in visual cortex (V1, N = 4 rats), and 17 cells in hippocampus (HPC, N = 8 rats).
353 The respiratory frequencies ranged from 1.44 Hz to 2.08 Hz (1.78±0.03 Hz, N = 25 rats).

354 In all these four areas, we found cells exhibiting respiration-related oscillations (RRo) in their
355 membrane potential (MP) and respiration-related (RR) spiking discharge, as shown in the raw
356 traces examples (Figure 2A). To highlight the RRo, the filtered respiratory signal (light gray)
357 was superimposed on the raw traces of the intracellular MP oscillations. In Figure 2B, the
358 power spectral density analysis of the MP signal (black PSD) showed a clear power peak at
359 the respiratory frequency (gray PSD) confirming that MP follows the respiratory rhythm in
360 these examples.

361 In order to properly characterize the relation between MP and respiratory rhythm, we
362 developed a cycle-by-cycle method for detecting the respiratory cycles during which MP
363 oscillated at the respiratory frequency (see Figure 1 and materials and methods for details).
364 We plotted the median of respiration-triggered membrane potential (Figure 2C bottom panels)
365 and the histograms of spiking occurrence during these cycles (Figure 2C top panels). In the
366 examples in Figure 2, MP RRo were large (median amplitude ± 95% confidence interval:
367 mPFC = 5.5±0.9 mV, S1 = 14.5±2.1 mV, V1 = 8.8±2.2 mV, HPC = 3.1±0.8 mV; Figure 2C
368 bottom panels), and APs occurrences were clearly related to respiratory cycle (top panels in
369 Figure 2C). Moreover, on these examples, MP RRo and firing pattern were similarly phase-

locked to respiration, suggesting a strong correlation between MP RRo and the associated firing. Indeed, spikes appeared on the top of the oscillation, where the MP exhibited the greatest depolarization.

In this way, we evidenced that a respiratory modulation could be expressed in the intracellular activity (MP and spiking) of cells in the four non-olfactory areas we recorded. The next step aimed to better characterize this MP respiratory modulation in each structure.

We first quantified the percentage of cells exhibiting MP RRo at resting membrane potential (Base polarity). As explained in Methods, we considered RRo only if the episode lasted at least 3 consecutive respiratory cycles. We measured in each cell, and in the 4 structures, the percentage of respiratory cycles during which an MP RRo was detected (Figure 3A), then we plotted the cumulative percentage of MP RRo cycles across cells for mPFC, S1 and HPC (Figure 3B). Since too few V1 recordings were available, V1 will not be included in the following comparative analyses. Additional shuffling statistics (see methods) revealed respiration-modulated cells represented 65.6% of cells (21/32) in mPFC, 70% (7/10) in S1, and 80% (8/10) in HPC. Therefore, at least 65% of the recorded cells in each structure presented a respiratory modulation. Additionally, the two cortical structures (mPFC and S1) presented slightly lower proportions of respiration-modulated cells than HPC. Specifically, the cumulative percentage curves (Figure 3B) showed that 20% of the cells in S1 and mPFC had more than 20% of their MP cycles modulated by respiration, about 20% of HPC cells had more than 75% of their cycles modulated.

As shown in Figure 3A1-4, the percentages of MP RRo cycles varied greatly from cell to cell within the same structure, from one structure to another. Indeed, if only the respiration-

modulated cells were considered (black bars without black cross), the percentage of cycles presenting an MP RRo ranged from 1.3% to 90.5% in mPFC (15.3±4.7%, N = 21 cells) and from 3.2% to 88.9% in HPC (29.5±11.4%, N = 8 cells), while it only extended from 3.9 to 33.3% in S1 (13.4±3.9%, N = 7 cells) (Figure 3C). Three neurons (one in mPFC and two in HPC) exhibited an extreme proportion of MP RRo cycles (more than 90%). The low percentage of MP RRo cycles for some cells was certainly due to our highly selective method for detecting RRo cycles (see material and methods). Due to the high variability between cells, no significant difference in proportion of MP RRo cycles between structures was observed (Figure 3C, Kruskal-Wallis test, $p = 0.53$, $H(2) = 1.24$).

To go one step further, we quantified for each respiration-modulated cell the average duration of RRo episodes (*i.e.*, the number of consecutive cycles in an MP RRo). As shown in Figure 3D, there was no significant difference in the duration of RRo episodes between structures (Figure 3D), (Kruskal-Wallis test, $p = 0.58$, $H(2) = 1.07$). In fact, the average number of consecutive MP RRo cycles was around five regardless of the structure (mPFC: 5.0±0.7, N = 21 cells; S1: 5.3±1.4, N = 7 cells; HPC: 5.8±1.2, N = 8 cells).

Taken together, these results showed that at least 65% of cells of each recorded structures could synchronize their MP oscillations with respiration. However, this respiratory modulation of MP was 1) highly variable both between structures and between cells, 2) very transient for most cells (with a mean episode duration of 5 cycles).

Next, to further explore the intrinsic dynamics of these RRo episodes, we studied both their amplitudes and phases. We first measured the amplitude of the median respiration-triggered MP (see material and methods for details) for each modulated cell (Figure 4A). Figure 4A revealed that amplitude of MP RRo was higher in S1 (10.7±2.4 mV, N = 7 cells) compared to

418 mPFC (4.0±0.5 mV, N = 21 cells) and HPC (4.4±0.9 mV, N = 8 cells) (Kruskal-Wallis test, p
419 = 0.01, H(2) = 9.1, *post hoc* Mann-Whitney U test S1–mPFC: p = 0.002 and S1-HPC: p =
420 0.02).

421

422 To pursue, we characterized the respiratory phase of the MP RRo. As already suggested by
423 the illustrative examples in Figure 2, the MP RRo phases were not unique. Indeed, while MP
424 exhibited maximal depolarized values around the transition phase between inspiration and
425 expiration in S1 and HPC examples (Figure 2C2 and 2C4), MP of mPFC and V1 examples
426 exhibited hyperpolarized values at this same respiratory phase (Figure 2C1 and 2C3). On the
427 whole dataset, we extracted, for each cell the phase of the most depolarized value of the
428 median MP RRo (see Figure 2, panels C-bottom for examples of median MP RRo). Figure 4B
429 shows for each structure the preferred phase for each cell. For mPFC, S1 and HPC these
430 phases seemed to be distributed according to two preferential values, one between 130-170
431 degree and the other between 315-340 degree. These ranges of values approximately
432 corresponded respectively to a period between the end of inspiration and the beginning of
433 expiration, *i.e.* near inspiration to expiration (I/E) transition (at 140 degree) and another
434 around the end of expiration, before expiration to inspiration (E/I) transition (at 0 degree).

435 Finally, we examined in detail the relationship between MP RRo and spiking discharge
436 (Respiration-Related (RR) or not). Table 1 presented the different association's possibilities
437 between MP (RRo or no-RRo) and discharge (RR discharge and no-RR discharge). To
438 construct this table, we considered the distribution of spikes as a function of respiratory phase
439 (see Figure 2C, top panels) using previously described method used in the olfactory bulb (34,
440 35) (see Material and Methods for details). For a given cell, we could compute two spike
441 distributions on the respiratory phase, one with the spikes occurring during period of MP RRo

and the other with the spikes occurring during MP no-RRo. The two spike distributions were then classified as either respiration-related (RR) discharge or non-respiration-related (no-RR) discharge. However, if the cell had no MP RRo period or if there were too few AP, spike distribution could not be classified, which explains the N in table 1 are lower than those observed in Figure 3. Table 1 summarized this classification across cells for each structure. It showed the percentages of each association between spiking discharge patterns (columns) and respiration-triggered MP types (lines). In mPFC and S1, the MP RRo was mostly associated with the RR discharge pattern (80% for both structures) and conversely the MP no-RRo was mostly associated with the No RR discharge pattern (71.4% and 85.7% respectively). The results for HPC did not show the same association profile. Indeed, only 25% of the MP RRo was associated with RR discharge pattern.

In summary, we showed that MP RRo were larger for cells in S1. The respiratory phases were mainly around I/E and E/I transitions for mPFC, S1 and HPC cells. Moreover, respiratory coupling between MP and spiking discharge was much more frequent in mPFC and S1 (80% each) than in HPC (25%).

Given the transient nature of MP RRo and their variability in amplitude and phase, we wondered whether parameters such as cell intrinsic state or local network state could influence respiratory modulation of MP.

Influence of intrinsic excitability and network activity on the respiratory modulation of membrane potential

Our second aim was then to examine to what extent MP RRo could be influenced by *(i)* intracellular excitability, and *(ii)* by local field potential (LFP) state.

(i) Effect of intracellular excitability.

First, we investigated the effect of excitability level on the probability for MP to be modulated by the respiration. Briefly, we tested two hyperpolarization levels (Hyp1 and Hyp2) and one depolarized level (Dep) by progressive direct intracellular DC current injection. As described in materials and methods, we used 3 criteria (firing, MP value, and injected current) to classify these excitability states.

The proportions of respiration-modulated cells (mPFC, S1 and HPC were pooled) were relatively stable between the four different excitability levels (Supplemental Figure S5A, Hyp2: 58% - 18 out 31 cells, Hyp1: 52% - 13 out of 25 cells, Base: 69% - 36 out of 52 cells, Dep: 62% - 13 out of 21 cells). Thus, considering the whole population, excitability level did not clearly influence the proportion of respiration-modulated cells.

Next, we compared the percentages of MP RRo cycles for a same cell when it was hyperpolarized from Base to Hyp1 level (Supplemental Figure S5B). This cell-by-cell analysis was necessary because of the great variability of MP RRo cycles proportion at base level within a same structure (*cf.* Figure 3). This analysis indicated that, the percentage of MP RRo cycles was reduced upon hyperpolarizing the cell (Base: 19.6±6.8%, Hyper1: 13.3±7.0%, Wilcoxon test $p = 0.01$, $Z = 7.0$, $N = 16$ cells)

These data showed that, although the internal excitability state had a weak influence on the proportion of respiration-modulated cells at the whole population level, moderate hyperpolarization of a cell decreased its percentage of MP RRo cycle.

(ii) Effect of LFP state.

As it is now well established that LFP in these brain structures can be modulated by respiration (25, 26), we then wondered how MP and LFP respiratory rhythms could interact. The raw traces in Figure 5A1 showed an example where neither MP nor LFP displayed RRo. Conversely, for the same recording, a few minutes later (Figure 5A2, after 2 min), respiratory frequency appeared simultaneously in MP and LFP signals. The similarity between both signals is highlighted when superimposing filtered respiratory signal (light gray traces on MP and LFP raw signals).

LFP RRo cycles were detected in the same way than MP RRo cycles, in order to be able to compare their temporal dynamics (see Methods). LFP RRo were found in the three structures. Figure 5B showed the average percentage of LFP RRo per recording (gray dots) and the percentages per structure (dark-gray squares). mPFC showed a significantly higher percentage of LFP RRo cycles than S1 (Kruskal-Wallis test, $p = 0.03$, $H(2) = 6.96$, *post hoc* Mann-Withney U test mPFC-S1, $p = 0.01$). The same tendency was observed with HPC, but significance was not reached (Mann-Withney U test mPFC-H, $p = 0.07$). In the same way as for the MP recordings, we quantified for each LFP recording the mean duration of LFP RRo episodes. The mean number of consecutive LFP RRo cycles (Figure 5C) was significantly higher for mPFC (10.6±2.2 cycles, N = 21 recordings) than for S1 (3.8±0.2 cycles, N = 5 recordings), and HPC (4.2±0.4 cycles, N = 4 recordings). (Kruskal Wallis $p = 7.10^{-3}$, $H(2) = 10.0$, *post hoc* Mann-Whitney U test mPFC-S1: $p = 0.005$, mPFC-HPC: $p = 0.02$)

We then investigated the extent to which LFP and MP respiration-modulation could be correlated. To do this, we calculated the percentage MP RRo cycles when the LFP exhibited RRo or not (Figure 5D). It became clear that, irrespective of the structure considered, the probability of the MP displaying RRo was higher when the LFP displayed RRo. For mPFC, the increased MP RRo probability when LFP switched from no RRo to RRo was significant (Wilcoxon test $p = 0.02$, $Z = 44$, N = 20 cells). HPC exhibited the same tendency (Wilcoxon

test, p = 0.07, Z= 0, n=4), and, to a lesser extent S1 also (Wilcoxon test, p = 0.14, Z= 1, n=4). Reciprocally, we wondered whether the probability of the LFP displaying RRo could be different when the MP displayed RRo or not (Figure 5E). We found that in mPFC, S1 and HPC, the probability of the LFP displaying RRo was higher when the MP displayed RRo, but this result was statistically significant only for mPFC (Wilcoxon test mPFC: p = 0.001, Z = 21, N = 20 cells). This confirmed that, most of the time, the respiratory modulation of a cell MP is coherent with the respiratory modulation of its network environment. Note that the lack of statistical significance in regions others than mPFC is probably due to the small sample size.

To summarize, we observed that MP and LFP are often respiratory co-modulated.

DISCUSSION

While many studies have recently evidenced a respiration-related activity in LFPs of many brain regions (21–26, 28, 29), our study is the first to describe respiratory-related oscillations in the MP activity in widespread brain areas, namely mPFC, S1, and HPC. We showed respiration-related oscillations of MP in a large proportion of cells (65.6% in mPFC, 70% in S1, and 80% in HPC). Before us, very sparse and scarce data existed reporting MP oscillations coherent with LFP respiration-related oscillation ((26, 29): 1 cell recorded in parietal cortex; (21): 3 cells out of 7 recorded in dentate gyrus after brainstem stimulation, (50) : 6 cells in parietal cortex). Our study goes further by comparing the probability of MP respiration-related oscillations in three different brain regions and by detailing how such oscillation could be influenced by excitability state or network activity. These results suggest that respiratory rhythm can entrain brain activity down to the membrane potential. In addition, we recorded in a preliminary study two prefrontal neurons whose membrane potential RRo was suppressed by ipsilateral nostril obstruction (Supplemental Figure S6). If extended, such results would definitively show that MP RRo in mPFC are entrained by respiratory nasal airflow. Contrarily to anesthetized animals, awake animals display various pattern of respiration. It has been shown that respiratory modulation is stronger for low frequency respiration (52–54), more precisely for short and deep inspirations (25, 55). During anesthesia, respiration tends to have a slow frequency and the inspiration tends to be shorter than the expiration. In our dataset, the mean respiratory frequency was 1.78Hz and the mean inspiration duration was 230ms. This inspiration duration is close to the optimal inspiration duration (100-200ms) previously observed during quiet wake (25, 55). Since the anesthesia brought the animal's respiration in a pattern close to the optimum, it could explain the extent of the respiratory modulation that we observed in this study. Finally, it would also be interesting to test whether the MP of cells in some brain structures could still be respiration

549 modulated in the absence of any OB afferents since it has been shown that cerebral activity
550 can also be modulated due to the presence of an intracerebral respiratory corollary discharge
551 originating from the brainstem (27).

552 Accumulating data showed that respiration can influence LFP from almost all brain areas (20,
553 25, 26), the unitary activity of several areas (22, 24, 27) and cognition (10, 13, 14). We
554 complementarily showed that membrane potential and action potential can be modulated by
555 respiration, and thus we reinforce the idea that respiratory rhythm could act as a common
556 clock for the brain. In this view, we expected the respiratory rhythm to synchronize
557 hyperpolarization and depolarization from distant neurons, facilitating their communication.
558 However, we rather observed that RRo displayed variable phase-locking to the respiration
559 (Figure 4B). Indeed, independently from the brain areas, neurons' depolarization tended to
560 phase-lock either to the inspiration-expiration transition or to the expiration-inspiration
561 transition. However, is this finding completely against the hypothesis of a communication
562 through respiratory rhythm? The same variability in phase-locking was observed in the
563 olfactory bulb (35, 40). In addition, Ackels and colleagues (40) showed mitral cells tended to
564 be depolarized during inspiration, while tufted cells depolarization occurred during expiration,
565 suggesting that the phase of respiratory rhythm could mediate information multiplexing. The
566 variability in phase-locking observed here (Figure 4B) suggests this multiplexing continues
567 beyond the olfactory bulb.

568 We first evidenced that the proportions of cells expressing MP respiration-related oscillations
569 were disparate between brain regions. In fact, cells were more likely to display RRo in HPC
570 than in S1 or mPFC (Figure 3B). Moreover, the amplitude of MP RRo was larger in S1 than
571 in other brain regions, at least in a sub-population of cells (see Figure 4A). Interestingly,
572 extracellularly recorded spiking activity in S1 has been previously described as rhythmically
573 correlated with respiration (22). This stronger relation between respiration and S1 barrel

cortex cells could have something to do with the fact that respiration binds different orofacial rhythms as whisking and sniffing particularly during olfactory search (7, 56, 57). Even if there is no whisker movement in the anesthetized preparation, olfactory and whisker cortices could be functionally linked since a crosswire between piriform and barrel cortices has been revealed in mouse brain slices after whiskers are trimmed, leading to a cross-modal sensory plasticity (58). Such a link could explain our observation.

We expected cells in mPFC to display more clearly respiration-related oscillations in their MP, given the strong modulation of LFP described in this region in the freely moving animal (25, 27, 59, 60). However, neither the duration of MP respiration-modulated episodes nor the amplitude of MP RRo is more pronounced in mPFC than in the three other areas. The fact that anesthetics have voltage-dependent effects on resting MP (61) could lower MP sensitivity to respiration. However, even in the awake head-fixed mouse, (24) reported that spiking discharges of neurons in mPFC are much less coupled to breathing than neurons in orbito-frontal cortex. This different probability of respiration-related oscillation between LFP and intracellular signals raises the question of a possible contamination of LFP signals by volume conduction coming from distant generators (62, 63).

Oppositely, we showed a very clear respiration-related activity in MP of HPC cells (80% of cells expressed RRo and 20% of them displayed at least 75% of modulated cycles). This probably reflects the strong relationship between olfactory and limbic structures. Very recently, Zhou et al. (64) reported that human hippocampal connectivity is stronger with olfactory cortex than other sensory cortices and that olfactory-hippocampal connectivity oscillates with nasal breathing. Interestingly, several recordings of HPC neurons exhibiting MP RRo revealed that, when emitted in bursts, action potentials were locked to the I/E transition point of respiratory cycle while single action potentials were more loosely distributed over the respiratory cycle (data not shown). It is commonly admitted that bursts

could facilitate synaptic transmission (65) and induce synaptic plasticity, LTP or LTD, depending on the theta oscillatory cycle phase of the burst (66). Furthermore, bursts increase detection of presynaptic events (67), thanks to their higher signal to noise ratio compared to single action potential. The fact that the MP of HPC cells could be paced by breathing could thus influence place cells coding notably during sniffing where respiratory and theta rhythms are in the same frequency range (25, 26).

We only recorded 4 cells in V1, 2 of them showed episodes of MP RRo. In these cells, the percentage of MP RRo did not exceed more than about 25% of total cycles. This confirms the observation that LFP in posterior areas are less susceptible to respiratory drive (25, 26). It is nevertheless interesting to observe that, even in a region as posterior as V1 and so improbably connected to the olfactory input, respiration can affect subthreshold activity.

We previously showed that the MP of mitral/tufted cells, the principal neurons of the olfactory bulb, is strongly respiration-modulated (35). We cannot compare the percentages of modulated cells between the non-olfactory structures recorded here and olfactory bulb neurons because we did not use the same experimental paradigm, neither the same detection method nor data processing. However, it can be noted that hyperpolarization of mPFC and S1 cells appears to reduce the number of cells exhibiting MP RRo. On the contrary, in the olfactory bulb, hyperpolarization induced an increase in the proportion of respiratory modulated cells, which could suggest a reversal potential of MP RRo more hyperpolarized in non-olfactory structures than in olfactory bulb. It would be necessary to undertake a fine characterization of the different types of RRo that may exist (as in mitral/tufted cells) in order to be able to formulate hypotheses. However, we could postulate that a greater inhibition would be implicated in the oscillatory dynamics of these non-olfactory cells, which is in line with recent findings (50). Indeed, it has been shown that inhibitory interneurons appear to be more respiratory modulated than pyramidal neurons (23, 27). It would be of great interest to

test the possibility that the consequence of a hyperpolarization (increase or a decrease of the respiratory modulation) would come from the fact that the respiratory influence could rather impinge on inhibitory interneurons (as it could be in mPFC) or on a balanced excitatory-inhibitory network (as in OB).

LFP RRo episodes were variable between regions, with duration up to 10 cycles in mPFC and between 3 and 6 cycles for other structures. This longer LFP RRo episode duration in mPFC is not surprising since several studies observed a particularly strong respiratory modulation in the prelimbic cortex. Then, the respiratory rhythm may take over more often than other rhythms. Alternating populations of cells could transiently express respiratory modulation in their MP resulting in a longer duration of LFP respiratory modulation. In other structures, the competition between several other LFP rhythms (such as slow rhythm or theta) probably does not favor the emergence of this rhythm. Additionally, for all the structures, the sensitivity of each individual cell MP to LFP respiratory modulation likely differs according to its excitability state, limiting episodes of MP RRo to short durations. This could be supported by our observation that cells could show less MP RRo when hyperpolarized (see Figure S5B).

Although our study focused on the respiratory rhythm, the influence of other LFP rhythms on cellular activity (MP and discharge) should not be ignored. For examples, in few cases, we observed a spiking discharge that was RR while MP displayed no RRo. We could suppose that if the spiking discharge is influenced by a rhythm twice slower or twice faster than the respiratory rhythm, they will appear locked on respiratory cycle on spike histograms. We also observed more complicated patterns with several rhythms nested. For example, on the MP spectrum analysis of Figure 2B3 we can distinguish a slow oscillation (around 1 Hz) which could compete with the respiratory rhythm.

Overall, our results evidenced a consequent proportion of RRo within electrophysiological signals, which could only have been revealed thanks to respiration co-recording. We evidenced a strong respiratory coupling between MP and spike discharge in PFC, S1 and to a lesser extent in HPC. Furthermore, MP and LFP RRo dynamics showed strong covariations. Even if our experiments in anesthetized animal are purely descriptive, our results show that, at very different places in the brain, the MP of neurons can be depolarized and hyperpolarized according to the respiratory rhythm. These findings contribute to the evidence that the respiratory rhythm could be used as a common clock to set the dynamics of large-scale networks on the same slow rhythm.

SUPPLEMENTAL MATERIAL

Figure S1: **Input resistance**

Figure S2: **Polarity states**

Figure S3: **AP waveform**

Figure S4: **Verification of possible correlations**

Figure S5: **Effect of excitability changes**

Figure S6: **Obstruction of the nostril**

Supplemental figures availability: https://doi.org/10.5281/zenodo.8165176

ACKNOWLEDGMENTS

We would like like to thank Marc Thévenet and Belkacem Messaoudi for providing technical assistance.

AUTHOR CONTRIBUTIONS

C.A. and N.B. conceived and designed research; M.J. and M.Z. performed experiments; M.J., N.F-T., S.G., C.A developed the RRo detection method; M.J analyzed data; M.J, N.F-T., N.B. and C.A. interpreted results of experiment; M.J. and C.A. prepared figures. M.J., N.B. and C.A. drafted manuscript; M.J., M.Z., N.F-T., N.B. and C.A. edited and revised manuscript; M.J., M.Z., N.F-T., S.G., N.B. and C.A approved final version of manuscript.

682 REFERENCES

683 1. **Heck DH**, **McAfee SS**, **Liu Y**, **Babajani-Feremi A**, **Rezaie R**, **Freeman WJ**,
684 **Wheless JW**, **Papanicolaou AC**, **Ruszinkó M**, **Sokolov Y**. Breathing as a fundamental
685 rhythm of brain function. *Front Neural Circuits* 10: 115, 2017.

686 2. **Heck DH**, **Kozma R**, **Kay LM**. The rhythm of memory: how breathing shapes
687 memory function. *J Neurophysiol* 122: 563–571, 2019.

688 3. **Maric V**, **Ramanathan D**, **Mishra J**. Respiratory regulation & interactions with
689 neuro-cognitive circuitry. *Neurosci Biobehav Rev* 112: 95–106, 2020.

690 4. **Zaccaro A**, **Piarulli A**, **Laurino M**, **Garbella E**, **Menicucci D**, **Neri B**, **Gemignani**
691 **A**. How breath-control can change your life: a systematic review on psycho-physiological
692 correlates of slow breathing. *Front Hum Neurosci* 12: 353, 2018.

693 5. **Cao Y**, **Roy S**, **Sachdev RN**, **Heck DH**. Dynamic correlation between whisking and
694 breathing rhythms in mice. *J Neurosci* 32: 1653–1659, 2012.

695 6. **Kurnikova A**, **Moore JD**, **Liao S-M**, **Deschênes M**, **Kleinfeld D**. Coordination of
696 orofacial motor actions into exploratory behavior by rat. *Curr Biol* 27: 688–696, 2017.

697 7. **Moore JD**, **Deschênes M**, **Furuta T**, **Huber D**, **Smear MC**, **Demers M**, **Kleinfeld**
698 **D**. Hierarchy of orofacial rhythms revealed through whisking and breathing. *Nature* 497:
699 205–210, 2013.

700 8. **Lu L**, **Cao Y**, **Tokita K**, **Heck DH**, **Boughter Jr JD**. Medial cerebellar nuclear
701 projections and activity patterns link cerebellar output to orofacial and respiratory behavior.
702 *Front Neural Circuits* 7: 56, 2013.

703 9. **Welzl H**, **Bureš J**. Lick-synchronized breathing in rats. *Physiol Behav* 18: 751–753,
704 1977.

705 10. **Arshamian A**, **Iravani B**, **Majid A**, **Lundström JN**. Respiration modulates olfactory
706 memory consolidation in humans. *J Neurosci* 38: 10286–10294, 2018.

707 11. **Waselius T**, **Wikgren J**, **Penttonen M**, **Nokia MS**. Breathe out and learn: expiration-
708 contingent stimulus presentation facilitates associative learning in trace eyeblink conditioning.
709 *Psychophysiology* 56: e13387, 2019.

710 12. **Nakamura NH**, **Fukunaga M**, **Oku Y**. Respiratory modulation of cognitive
711 performance during the retrieval process. *PloS One* 13: e0204021, 2018.

712 13. **Perl O**, **Ravia A**, **Rubinson M**, **Eisen A**, **Soroka T**, **Mor N**, **Secundo L**, **Sobel N**.
713 Human non-olfactory cognition phase-locked with inhalation. *Nat Hum Behav* 3: 501–512,
714 2019.

715 14. **Zelano C**, **Jiang H**, **Zhou G**, **Arora N**, **Schuele S**, **Rosenow J**, **Gottfried JA**. Nasal

716 respiration entrains human limbic oscillations and modulates cognitive function. *J Neurosci*
717 36: 12448–12467, 2016.

718 15. **Grund M**, **Al E**, **Pabst M**, **Dabbagh A**, **Stephani T**, **Nierhaus T**, **Gaebler M**,
719 **Villringer A**. Respiration, heartbeat, and conscious tactile perception. *J Neurosci* 42: 643–
720 656, 2022.

721 16. **Iwabe T**, **Ozaki I**, **Hashizume A**. The respiratory cycle modulates brain potentials,
722 sympathetic activity, and subjective pain sensation induced by noxious stimulation. *Neurosci*
723 *Res* 84: 47–59, 2014. doi: 10.1016/j.neures.2014.03.003.

724 17. **Li S**, **Park W-H**, **Borg A**. Phase-dependent respiratory-motor interactions in reaction
725 time tasks during rhythmic voluntary breathing. *Motor Control* 16: 493–505, 2012.

726 18. **Li S**, **Laskin JJ**. Influences of ventilation on maximal isometric force of the finger
727 flexors. *Muscle Nerve* 34: 651–655, 2006. doi: https://doi.org/10.1002/mus.20592.

728 19. **Park H-D**, **Barnoud C**, **Trang H**, **Kannape OA**, **Schaller K**, **Blanke O**. Breathing is
729 coupled with voluntary action and the cortical readiness potential. *Nat Commun* 11: 1–8,
730 2020.

731 20. **Herrero JL**, **Khuvis S**, **Yeagle E**, **Cerf M**, **Mehta AD**. Breathing above the brain
732 stem: volitional control and attentional modulation in humans. .

733 21. **Yanovsky Y**, **Ciatipis M**, **Draguhn A**, **Tort AB**, **Brankačk J**. Slow oscillations in
734 the mouse hippocampus entrained by nasal respiration. *J Neurosci* 34: 5949–5964, 2014.

735 22. **Ito J**, **Roy S**, **Liu Y**, **Cao Y**, **Fletcher M**, **Lu L**, **Boughter JD**, **Grün S**, **Heck DH**.
736 Whisker barrel cortex delta oscillations and gamma power in the awake mouse are linked to
737 respiration. *Nat Commun* 5: 3572, 2014. doi: 10.1038/ncomms4572.

738 23. **Biskamp J**, **Bartos M**, **Sauer J-F**. Organization of prefrontal network activity by
739 respiration-related oscillations. *Sci Rep* 7: 1–11, 2017.

740 24. **Köszeghy Á**, **Lasztóczi B**, **Forro T**, **Klausberger T**. Spike-timing of orbitofrontal
741 neurons is synchronized with breathing. *Front Cell Neurosci* 12: 105, 2018.

742 25. **Girin B**, **Juventin M**, **Garcia S**, **Lefèvre L**, **Amat C**, **Fourcaud-Trocmé N**,
743 **Buonviso N**. The deep and slow breathing characterizing rest favors brain respiratory-drive.
744 *Sci Rep* 11: 1–15, 2021.

745 26. **Tort ABL**, **Ponsel S**, **Jessberger J**, **Yanovsky Y**, **Brankačk J**, **Draguhn A**. Parallel
746 detection of theta and respiration-coupled oscillations throughout the mouse brain. *Sci Rep* 8:
747 6432, 2018. doi: 10.1038/s41598-018-24629-z.

748 27. **Karalis N**, **Sirota A**. Breathing coordinates cortico-hippocampal dynamics in mice
749 during offline states. *Nat Commun* 13: 1–20, 2022.

750 28. **Liu Y**, **McAfee SS**, **Heck DH**. Hippocampal sharp-wave ripples in awake mice are

entrained by respiration. *Sci Rep* 7: 1–9, 2017.

29. **Zhong W**, **Ciatipis M**, **Wolfenstetter T**, **Jessberger J**, **Müller C**, **Ponsel S**, **Yanovsky Y**, **Brankačk J**, **Tort AB**, **Draguhn A**. Selective entrainment of gamma subbands by different slow network oscillations. *Proc Natl Acad Sci* 114: 4519–4524, 2017.

30. **Grosmaitre X**, **Santarelli LC**, **Tan J**, **Luo M**, **Ma M**. Dual functions of mammalian olfactory sensory neurons as odor detectors and mechanical sensors. *Nat Neurosci* 10: 348–354, 2007.

31. **Lockmann AL**, **Laplagne DA**, **Leão RN**, **Tort AB**. A respiration-coupled rhythm in the rat hippocampus independent of theta and slow oscillations. *J Neurosci* 36: 5338–5352, 2016.

32. **Buonviso N**, **Amat C**, **Litaudon P**. Respiratory modulation of olfactory neurons in the rodent brain. *Chem Senses* 31: 145–154, 2006.

33. **Buonviso N**, **Amat C**, **Litaudon P**, **Roux S**, **Royet J-P**, **Farget V**, **Sicard G**. Rhythm sequence through the olfactory bulb layers during the time window of a respiratory cycle. *Eur J Neurosci* 17: 1811–1819, 2003.

34. **Cenier T**, **David F**, **Litaudon P**, **Garcia S**, **Amat C**, **Buonviso N**. Respiration-gated formation of gamma and beta neural assemblies in the mammalian olfactory bulb. *Eur J Neurosci* 29: 921–930, 2009.

35. **Briffaud V**, **Fourcaud-Trocmé N**, **Messaoudi B**, **Buonviso N**, **Amat C**. The relationship between respiration-related membrane potential slow oscillations and discharge patterns in mitral/tufted cells: what are the rules? *PLoS One* 7: e43964, 2012.

36. **Courtiol E**, **Amat C**, **Thevenet M**, **Messaoudi B**, **Garcia S**, **Buonviso N**. Reshaping of bulbar odor response by nasal flow rate in the rat. *PLoS One* 6: e16445, 2011.

37. **David FO**, **Hugues E**, **Cenier T**, **Fourcaud-Trocmé N**, **Buonviso N**. Specific entrainment of mitral cells during gamma oscillation in the rat olfactory bulb. *PLoS Comput Biol* 5: e1000551, 2009.

38. **Cury KM**, **Uchida N**. Robust odor coding via inhalation-coupled transient activity in the mammalian olfactory bulb. *Neuron* 68: 570–585, 2010.

39. **Gschwend O**, **Beroud J**, **Carleton A**. Encoding odorant identity by spiking packets of rate-invariant neurons in awake mice. *PloS One* 7: e30155, 2012.

40. **Ackels T**, **Jordan R**, **Schaefer AT**, **Fukunaga I**. Respiration-locking of olfactory receptor and projection neurons in the mouse olfactory bulb and its modulation by brain state. *Front Cell Neurosci* 14: 220, 2020.

41. **Fourcaud-Trocmé N**, **Briffaud V**, **Thévenet M**, **Buonviso N**, **Amat C**. In vivo beta and gamma subthreshold oscillations in rat mitral cells: origin and gating by respiratory dynamics. *J Neurophysiol* 119: 274–289, 2018.

42. **Courtiol E**, **Hegoburu C**, **Litaudon P**, **Garcia S**, **Fourcaud-Trocmé N**, **Buonviso N**. Individual and synergistic effects of sniffing frequency and flow rate on olfactory bulb activity. *J Neurophysiol* 106: 2813–2824, 2011.

43. **Esclassan F**, **Courtiol E**, **Thévenet M**, **Garcia S**, **Buonviso N**, **Litaudon P**. Faster, deeper, better: the impact of sniffing modulation on bulbar olfactory processing. *PloS One* 7: e40927, 2012.

44. **Oka Y**, **Takai Y**, **Touhara K**. Nasal airflow rate affects the sensitivity and pattern of glomerular odorant responses in the mouse olfactory bulb. *J Neurosci* 29: 12070–12078, 2009.

45. **Courtiol E**, **Buonviso N**, **Litaudon P**. Odorant features differentially modulate beta/gamma oscillatory patterns in anterior versus posterior piriform cortex. *Neuroscience* 409: 26–34, 2019.

46. **Litaudon P**, **Amat C**, **Bertrand B**, **Vigouroux M**, **Buonviso N**. Piriform cortex functional heterogeneity revealed by cellular responses to odours. *Eur J Neurosci* 17: 2457–2461, 2003.

47. **Litaudon P**, **Garcia S**, **Buonviso N**. Strong coupling between pyramidal cell activity and network oscillations in the olfactory cortex. *Neuroscience* 156: 781–787, 2008.

48. **Miura K**, **Mainen ZF**, **Uchida N**. Odor representations in olfactory cortex: distributed rate coding and decorrelated population activity. *Neuron* 74: 1087–1098, 2012.

49. **Carlson KS**, **Dillione MR**, **Wesson DW**. Odor-and state-dependent olfactory tubercle local field potential dynamics in awake rats. *J Neurophysiol* 111: 2109–2123, 2014.

50. **Jung F**, **Witte V**, **Yanovsky Y**, **Klumpp M**, **Brankack J**, **Tort AB**, **Dr. Draguhn A**. Differential modulation of parietal cortex activity by respiration and $þeta$-oscillations. .

51. **Roux SG**, **Garcia S**, **Bertrand B**, **Cenier T**, **Vigouroux M**, **Buonviso N**, **Litaudon P**. Respiratory cycle as time basis: An improved method for averaging olfactory neural events. *J Neurosci Methods* 152: 173–178, 2006. doi: 10.1016/j.jneumeth.2005.09.004.

52. **Pager J**. Respiration and olfactory bulb unit activity in the unrestrained rat: statements and reappraisals. *Behav Brain Res* 16: 81–94, 1985.

53. **Kay LM**, **Laurent G**. Odor-and context-dependent modulation of mitral cell activity in behaving rats. *Nat Neurosci* 2: 1003–1009, 1999.

54. **Sheriff A**, **Pandolfi G**, **Nguyen VS**, **Kay LM**. Long-range respiratory and theta oscillation networks depend on spatial sensory context. *J Neurosci* 41: 9957–9970, 2021.

55. **Juventin M**, **Ghibaudo V**, **Granget J**, **Amat C**, **Courtiol E**, **Buonviso N**. Respiratory influence on brain dynamics: the preponderant role of the nasal pathway and deep slow regime. *Pflüg Arch - Eur J Physiol* 475: 23–35, 2023. doi: 10.1007/s00424-022-02722-7.

56. **Kleinfeld D**, **Moore JD**, **Wang F**, **Deschênes M**. The brainstem oscillator for whisking and the case for breathing as the master clock for orofacial motor actions. In: *Cold Spring Harbor symposia on quantitative biology*. Cold Spring Harbor Laboratory Press, 2014, p. 29–39.

57. **Ranade S**, **Hangya B**, **Kepecs A**. Multiple Modes of Phase Locking between Sniffing and Whisking during Active Exploration. *J Neurosci* 33: 8250–8256, 2013. doi: 10.1523/JNEUROSCI.3874-12.2013.

58. **Ye B**, **Huang L**, **Gao Z**, **Chen P**, **Ni H**, **Guan S**, **Zhu Y**, **Wang J-H**. The functional upregulation of piriform cortex is associated with cross-modal plasticity in loss of whisker tactile inputs. .

59. **Bagur S**, **Lefort JM**, **Lacroix MM**, **de Lavilléon G**, **Herry C**, **Chouvaeff M**, **Billand C**, **Geoffroy H**, **Benchenane K**. Breathing-driven prefrontal oscillations regulate maintenance of conditioned-fear evoked freezing independently of initiation. *Nat Commun* 12: 1–15, 2021.

60. **Dupin M**, **Garcia S**, **Boulanger-Bertolus J**, **Buonviso N**, **Mouly A-M**. New insights from 22-kHz ultrasonic vocalizations to characterize fear responses: relationship with respiration and brain oscillatory dynamics. *Eneuro* 6, 2019.

61. **MacIver MB**, **Kendig JJ**. Anesthetic effects on resting membrane potential are voltage-dependent and agent-specific. *Anesthesiology* 74: 83–88, 1991.

62. **Kajikawa Y**, **Schroeder CE**. How local is the local field potential? *Neuron* 72: 847–858, 2011.

63. **Parabucki A**, **Lampl I**. Volume conduction coupling of whisker-evoked cortical LFP in the mouse olfactory bulb. *Cell Rep* 21: 919–925, 2017.

64. **Zhou G**, **Olofsson JK**, **Koubeissi MZ**, **Menelaou G**, **Rosenow J**, **Schuele SU**, **Xu P**, **Voss JL**, **Lane G**, **Zelano C**. Human hippocampal connectivity is stronger in olfaction than other sensory systems. *Prog Neurobiol* 201: 102027, 2021.

65. **Miles R**. Synaptic excitation of inhibitory cells by single CA3 hippocampal pyramidal cells of the guinea-pig in vitro. *J Physiol* 428: 61–77, 1990.

66. **Huerta PT**, **Lisman JE**. Bidirectional synaptic plasticity induced by a single burst during cholinergic theta oscillation in CA1 in vitro. *Neuron* 15: 1053–1063, 1995.

67. **Sherman SM**. Tonic and burst firing: dual modes of thalamocortical relay. *Trends Neurosci* 24: 122–126, 2001.

FIGURE LEGENDS:

Figure 1 Description of the RRo detection method. Common color code: real data measurements are in red, median signals are in green, surrogate measurements are in light blue. **A)** Schematic description of the processing chain. **B)** Detailed description of the processing chain. **B.1)** Preprocessed membrane potential (APs removal and deformation to respiratory phase) along 7 respiratory cycles. **B.2)** Encoding of the 4 windows associated to the 7 previous cycles (B.1). The encoding of the window 118 is detailed in the panel C. Windows 118 to 120 are found to be related to respiration (in red), while the window 121 is not (blue). The median signals associated to each window are shown in green. **B.3)** Encoding of the similarity associated with the 4 windows presented above (B.2). The encoding of the cycle 118 as part of the windows 118 is detailed in panel D. Individual cycles similar to the window they belong to are shown in black. Dissimilar cycles are in gray. Cycles that are not tested (because the associated window is not respiration-related) are in light gray. **B.4)** Cycle-by-cycle encoding. The score of a cycle corresponds to the number of times this cycle is found similar to the waveform of a respiration-related window. For example, the cycle 121 is found similar to 3 respiration-related window waveforms and thus reached the score of 3 (B.3). Cycles with score of 3 or 4 are classified as RRo. Cycles with score of 2 are classified as undetermined. Cycles with score of 0 or 1 are classified as no RRo. **C)** Detailed detection on local windows. **C.1)** Construction of surrogates. The left-hand column corresponds to actual cycles. The right-hand column corresponds to surrogates. Surrogates are constructed in two steps. First, the cycles are randomly paired (here cycle 118 with 119, and 121 with 120). Then, the cycles are phase-shifted, so that they are two by two in phase opposition. **C.2)** The median signal of the 4 actual cycle, on the left, or of the 4 surrogates, on the right. The red, respectively the light-blue, line indicates the amplitude of the actual signal, respectively the surrogate **C3.)** Distribution of the surrogate amplitudes. Blue bars represent the distribution of surrogate amplitudes. Black arrow highlights the p-values (95^{th} percentiles). Red arrow

highlights the amplitude of actual data (C.2 left). **D)** Detailed verification of the similarity. **D.1)** To assess the similarity between individual cycles (gray) and the local window oscillation (green), we compute the scalar product of these z-scored signals. **D.2.)** Distribution of the surrogate scalar products. Blue bars represent the distribution of surrogate scalar products. The black arrow highlights the p-values (95^{th} percentiles). The red arrow highlights the scalar product of actual data (D.1 left).

Figure 2 : Intracellular activity of widespread brain areas correlates with respiratory rhythm. A) Raw traces of intracellular activity from mPFC, S1, V1 and HPC (respectively subpanels 1, 2, 3, 4). Top trace: intracellular raw trace in black, overlaid with a filtered (3 Hz low pass) respiratory signal, in gray, which has been time-shifted to highlight MP RRo. Mid trace: Respiratory signal. Bottom: Respiratory phase, with gray bars representing inspiration phases, white bars representing expiration phases. Time scale bar = 1s, amplitude scale bar = 10 mV. E = expiration, I = inspiration. AP have been truncated. **B)** MP (black) and respiratory signal (gray) power density spectrum over the 4s of signal presented in A. Arrow heads highlight 1^{st} harmonic of the spectrum. **C)** Respiration-triggered AP firing histogram (top) and respiration triggered MP (bottom). Data of respiration-triggered figures are extracted from several cycles during which MP is identified as correlated with respiration. Cycles and AP numbers are indicated on the right top. To visually reinforce oscillatory behavior, plots have been duplicated. Respiratory phase is reminded in between the two respiration-triggered figures. Bottom: respiration triggered MP where black line corresponds to the median, shaded areas delineate the 25^{th} and 75^{th} percentiles.

Figure 3 : A significant number of cells in each structure exhibit MP RRo, yet individual episodes are short. Only recordings at basal MP are considered. **A)** Distribution of MP encoding by cell in mPFC, S1, V1 and HPC (respectively subpanels 1, 2, 3, 4). Black, gray and white, bars correspond to the probability of RRo cycles, undetermined cycles and no RRo cycles respectively. The total number of respiratory cycles recorded in each cell is indicated at the top of the corresponding bar. Black crosses indicated cells which are not considered as modulated by respiration despite showing some MP RRo (see methods) **B)** Cumulative distribution of RRo percentages of each structure. Blue, orange and pink curves correspond to mPFC, S1 and HPC respectively. **C)** MP RRo probabilities across structures. Gray dots represent MP RRo probability for individual cells, blue squares represent the mean by structure and black lines represent SEM. Only respiration-modulated cells are considered. No significant differences are observed (Kruskal-Wallis test, $p = 0.53$, $H(2) = 1.24$, $N_{mPFC} = 21$, $N_{S1} = 7$, $N_{HPC} = 8$). **D)** MP RRo episodes duration across structures. Gray dots represent mean MP RRo episode duration of individual cells, blue squares represent the mean by structure and black lines represent SEM. The same cell pool as in B is used. No significant differences are observed (Kruskal-Wallis test, $p = 0.58$, $H(2) = 1.07$, $N_{mPFC} = 21$, $N_{S1} = 7$, $N_{HPC} = 8$).

Figure 4 : Phase and amplitude characterization of MP RRo. Only recordings at basal MP and respiration-modulated cells are considered. A) Amplitude of MP RRo by structures. Gray dots represent MP RRo amplitude of individual cells, dark gray squares represent the mean by structure and black lines represents SEM. Significant differences are observed (Kruskal-Wallis test, $p = 0.01$, $H(2) = 9.1$, $N_{mPFC} = 21$, $N_{S1} = 7$, $N_{HPC} = 8$). *Post hoc* two-sided Mann-Whitney U test reveals amplitude of MP RRo is higher in S1 cells than in mPFC ($p = 0.002$) and HPC ($p = 0.02$). B) Preferred respiratory phase MP RRo by structures. Preferred phases

930 are presented on a trigonometric circle, phase progression is anticlockwise. Shaded and white
931 areas, correspond respectively to inspirations and expirations.

932

933 **Figure 5: MP RRo probability increases when RRo are concomitantly present in LFP.**
934 Only recordings at basal MP are considered. In addition, for B and C, only recording with
935 respiration-modulated LFP are considered. While for D and E, only recordings with both
936 respiration-modulated LFP and cells are considered. **A)** MP (Top), respiratory signal (mid)
937 and LFP (bottom) raw traces of the same cell when LFP and MP do not display RRo (A1) and
938 two minutes later when LFP and MP display RRo (A2). On A2 panel, light gray traces show
939 filtered and time-shifted respiratory signal superimposed on MP and LFP traces. Time scale
940 bar: 1s. **B)** LFP RRo probability by structures. Gray points represent LFP RRo probability,
941 dark gray squares represent the mean by structure and black lines represent SEM. Significant
942 differences are observed (Kruskal-Wallis test, $p = 0.03$, $H(2) = 6.96$, $N_{mPFC} = 21$, $N_{S1} = 5$,
943 $N_{HPC} = 4$). The LFP in mPFC presents more RRo than S1 (Mann-Withney U test, $p = 0.01$).
944 **C)** LFP RRo episode duration by structures. Gray dots represent mean LFP RRo duration of
945 individual traces, dark gray squares represent the mean by structure and black lines represent
946 SEM. The same pool of traces as in B is used. Significant differences are observed (Kruskal-
947 Wallis test, $p = 7.10^{-3}$, $H(2) = 10.0$, $N_{mPFC} = 21$, $N_{S1} = 5$, $N_{HPC} = 4$). The mPFC presents
948 longer LFP RRo episodes than S1 (Mann-Whitney U test, $p = 0.005$) and HPC (Mann-
949 Whitney U test, $p = 0.02$). **D)** Conditional probability of MP RRo given LFP dynamics. The
950 columns “LFP RRo” represent the probability to observe MP RRo when LFP is also RRo. On
951 the other hand, the columns “other LFP” represent MP RRo probability when LFP is no RRo.
952 In the mPFC, the probability of MP RRo increases when LFP is RRo (Wilcoxon test, $p =$
953 0.02, $Z= 44$, $n=20$). S1 (Wilcoxon test, $p = 0.14$, $Z= 1$, $n=4$) and HPC (Wilcoxon test, $p =$
954 0.07, $Z= 0$, $n=4$) presented the same tendency. **E)** Conditional probability of LFP RRo given

MP dynamics. The columns “MP RRo” represent the probability to observe LFP RRo when MP is also RRo. On the other hand, the columns “other MP” represent the probability of LFP RRo when MP is no RRo. In the mPFC, LFP RRo probability increases when MP is RRo (Wilcoxon test, $p = 0.002$, $Z=21$, $n=20$). S1 (Wilcoxon test, $p = 0.14$, $Z= 1$, $n=4$) and HPC (Wilcoxon test, $p = 0.07$, $Z= 0$, $n=4$) presented the same tendency.

961

962 TABLE:

963 **Table 1: mPFC and S1 show stronger coupling between MP oscillations and spiking**

964 **than hippocampus.**

Area	MP activity		RR discharge	No RR discharge	Total cells
mPFC	RRo	N_{cell} %	4 80%	1 20%	5
	no RRo	N_{cell} %	6 28.6%	15 71.4%	21
S1	RRo	N_{cell} %	4 80%	1 20%	5
	no RRo	N_{cell} %	1 14.3%	6 85.7%	7
HPC	RRo	N_{cell} %	1 25%	3 75%	4
	no RRo	N_{cell} %	3 37.5%	5 62.5%	8

965

966 For each cell, spikes are sorted according to whether they occurred during MP RRo or no MP
967 RRo. Respiration-triggered discharge histograms are computed for both categories. The
968 histograms are then classified as either RR discharge or no RR discharge. Results are
969 presented for each area and each MP activity. The line "N_{cell}" represents the number of cells in
970 each discharge class. It should be be noted that spike distributions with too few spikes were
971 not considered here or some cells never displayed MP RRo with spikes. Consequently, the
972 total number of cells in the lines 'RRo' are lower than the number of respiration-modulated
973 cells (showed in Figure 3) and the total number of cells in the lines 'no RRo' are lower than
974 the total number of cells. The line "%" represents the percentage of cells in each discharge
975 category relative to the total number of cells associated to an MP RRo category.

976

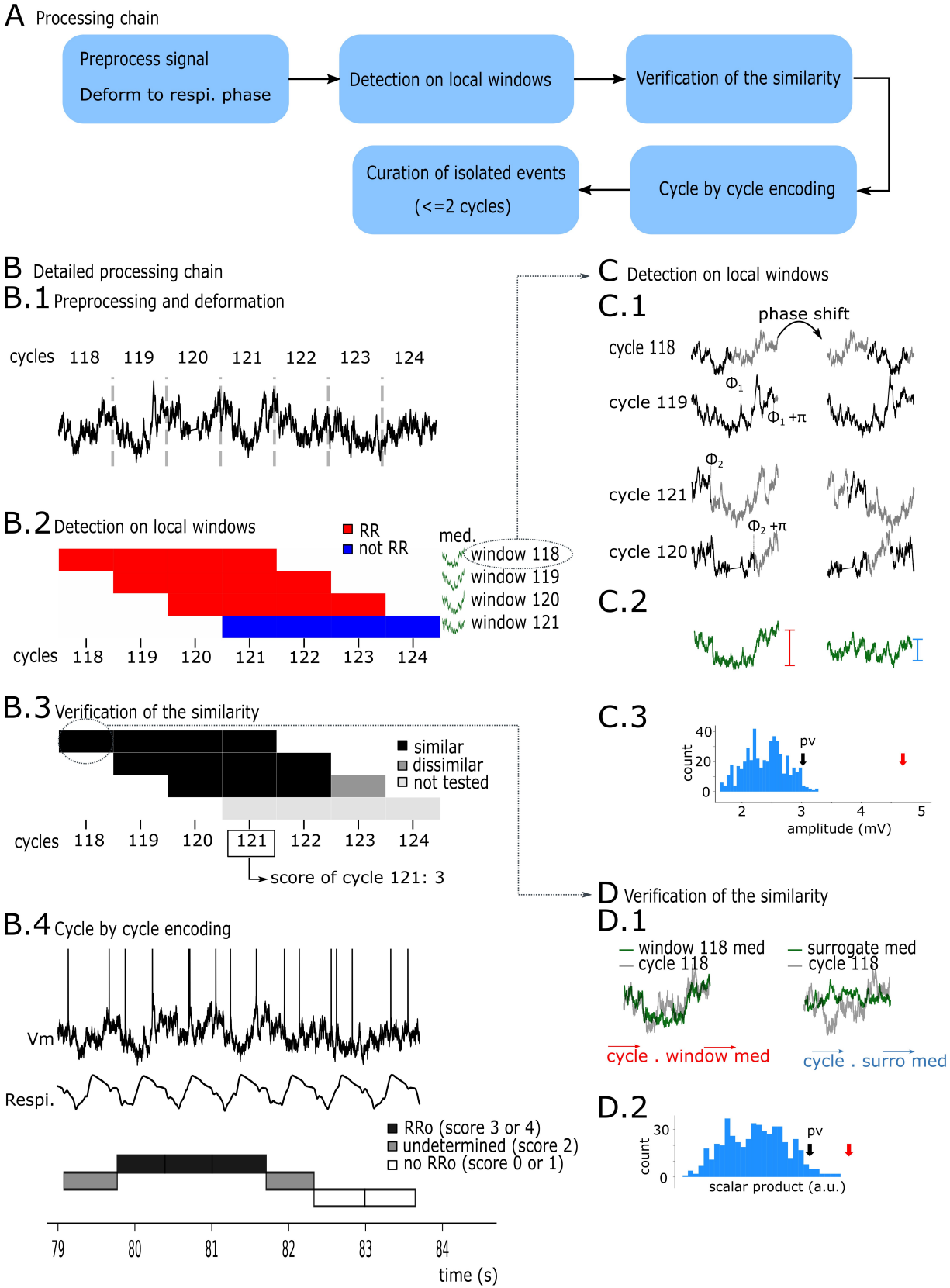

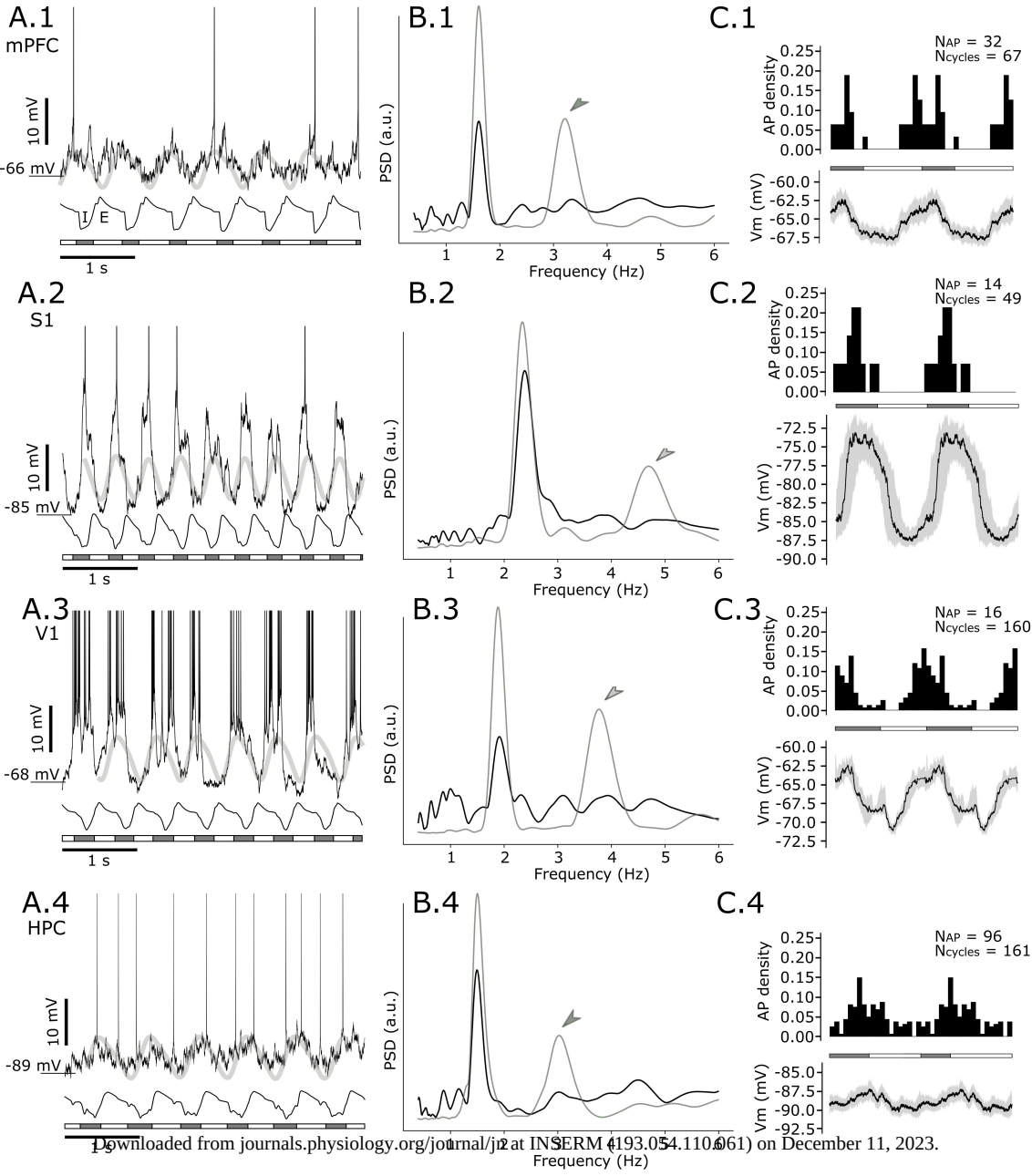

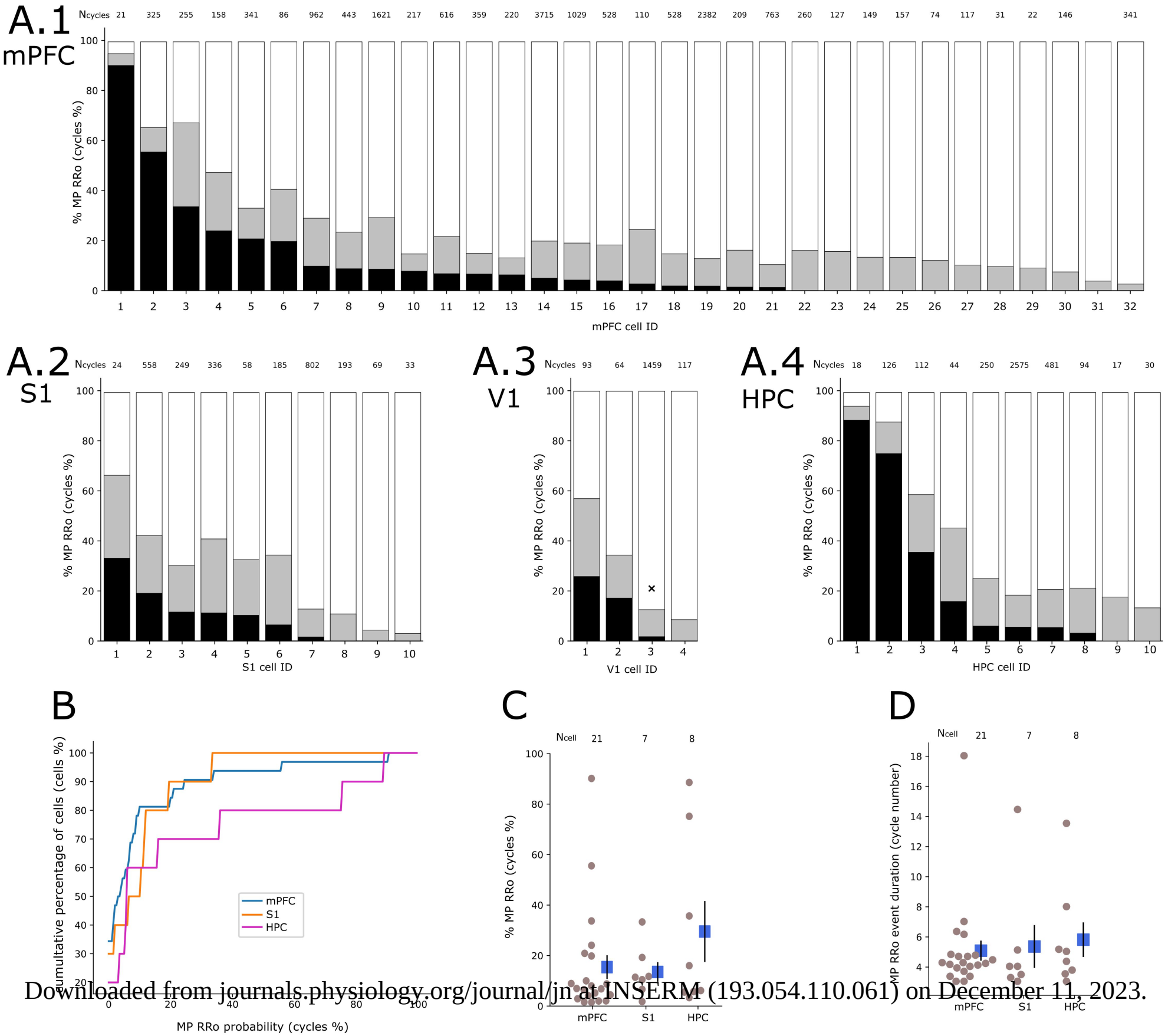

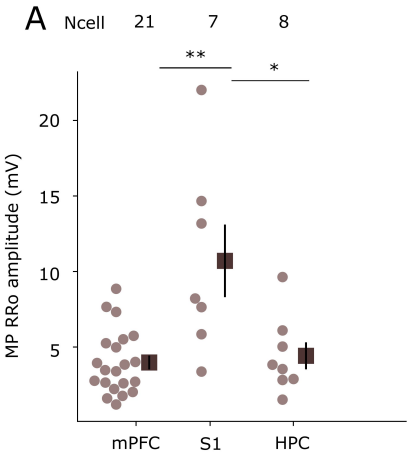

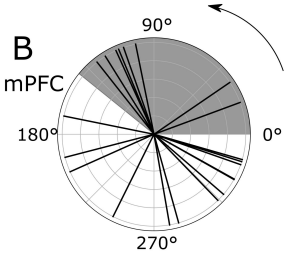

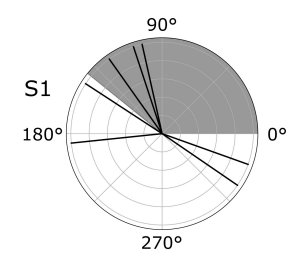

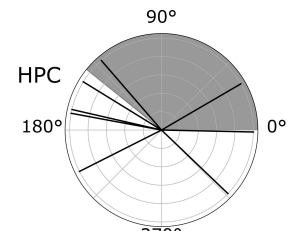

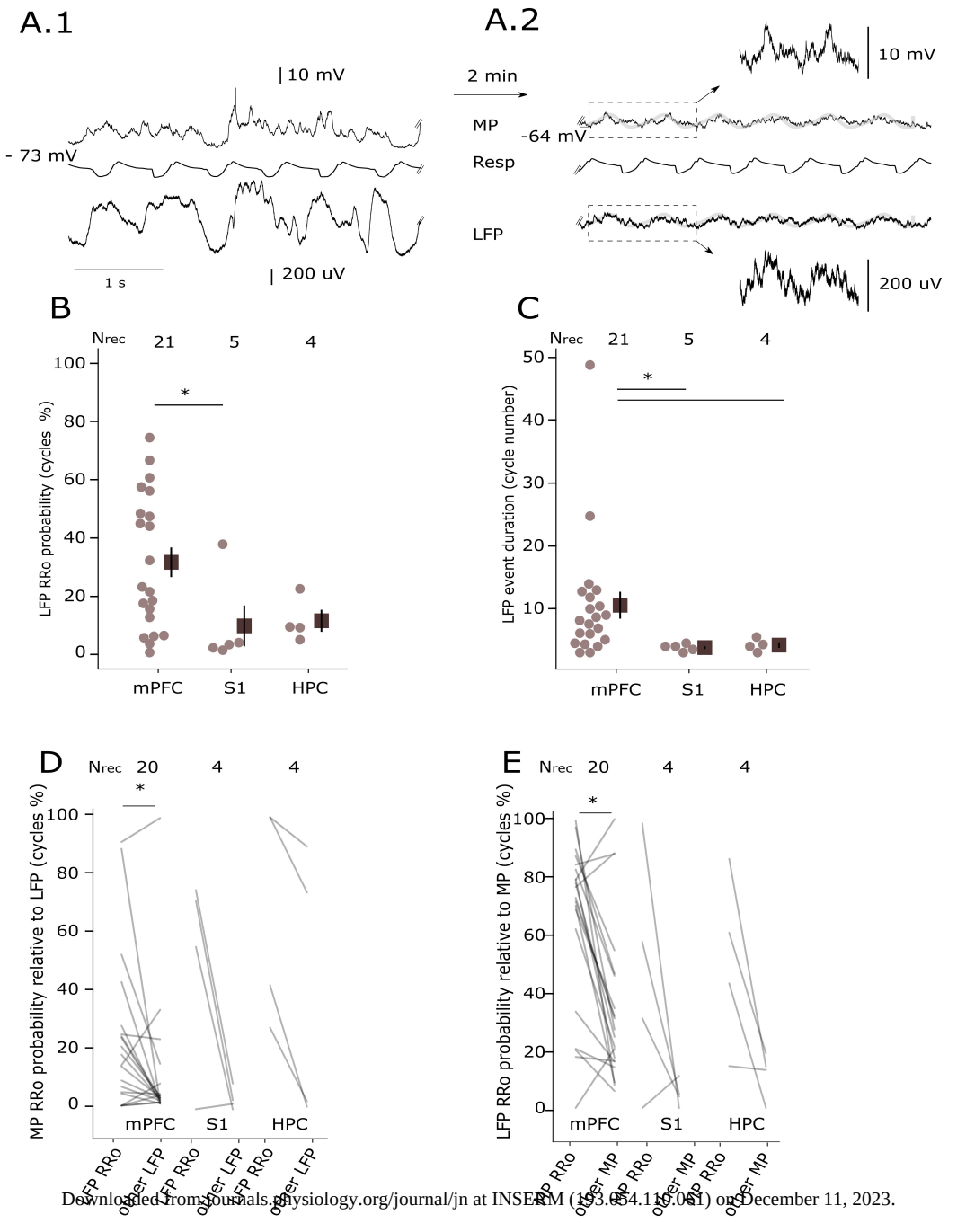

Table 1: mPFC and S1 show stronger coupling between MP oscillations and spiking than hippocampus.

Area	MP activity		RR discharge	No RR discharge	Total cells
mPFC	RRo	N_{cell} %	4 80%	1 20%	5
	no RRo	N_{cell} %	6 28.6%	15 71.4%	21
S1	RRo	N_{cell} %	4 80%	1 20%	5
	no RRo	N_{cell} %	1 14.3%	6 85.7%	7
HPC	RRo	N_{cell} %	1 25%	3 75%	4
	no RRo	N_{cell} %	3 37.5%	5 62.5%	8

For each cell, spikes are sorted according to whether they occurred during MP RRo or no MP RRo. Respiration-triggered discharge histograms are computed for both categories. The histograms are then classified as either RR discharge or no RR discharge. Results are presented for each area and each MP activity. The line "N_{cell}" represents the number of cells in each discharge class. It should be be noted that spike distributions with too few spikes were not considered here or some cells never displayed MP RRo with spikes. Consequently, the total number of cells in the lines 'RRo' are lower than the number of respiration-modulated cells (showed in **Error! Reference source not found.**) and the total number of cells in the lines 'no RRo' are lower than the total number of cells. The line "%" represents the percentage of cells in each discharge category relative to the total number of cells associated to an MP RRo category.